Journal of Energy Storage 77 (2024) 109971

Contents lists available at ScienceDirect

Journal of Energy Storage

journal homepage: www.elsevier.com/locate/est

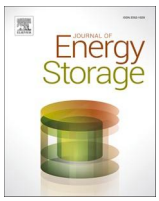

Research papers

Design approach for electric vehicle battery packs based on experimentally tested multi-domain models

Clemente Capasso [a,*], Luigi Iannucci [b], Stanislao Patalano [b], Ottorino Veneri [a], Ferdinando Vitolo [b]

[a] National Research Council of Italy, Institute of Sciences and Technologies for Sustainable Energy and Mobility, Italy
[b] University of Naples Federico II, Fraunhofer J-Lab IDEAS, Department of Industrial Engineering, Italy

ARTICLE INFO

Keywords:
Battery electric vehicles
Electro-thermal analysis
Multi-domain modelling

ABSTRACT

This work proposes a multi-domain modelling methodology to support the design of new battery packs for automotive applications. The methodology allows electro-thermal evaluation of different spatial arrangements of the storage cells by exploiting the implementation of numerical and geometrical battery pack models. Concerning the case study on Li-NMC battery technology, the study has completed the electro-thermal characterization of the storage cells starting from the collected experimental data, considering both the thermal interactions among cells and the effects of the state of health. This work also investigates the effects of forced air-cooling systems focusing on battery pack hot spots and temperature distributions. The results show a good fit between numerical models and data obtained from single-cell experiments. The virtual linking of geometric and numerical lumped-parameter models proved to be effective in rapid battery pack prototyping for electric vehicles, helping designers and manufacturers find suitable solutions for specific automotive applications.

1. Introduction

In recent years, vehicle manufacturers have shifted their attention towards eco-friendly transport systems mainly based on Electric Vehicles (EVs), which appear to be the most promising low-emission technologies available on the market. Thanks to recent advancements in Lithium-ion battery technology, electric vehicle storage systems have greatly improved in terms of energy and power density, which have reached values of 250 Wh/kg and 400 W/L [1–3], allowing the diffusion of electric vehicles in the global transportation market. EVs have many benefits, which are mainly the absence of local exhaust emissions, good performance (thanks to the torque/speed characteristics of electric propulsion systems), and low mechanical maintenance requirements [4–6].

Despite the above advantages of battery technology, researchers and developers must still address various issues in the coming years. The performances of Lithium-ion cells are dependent on several parameters such as State of Charge (SoC), State of Health (SoH), charging/discharging current values, and operative temperature [7,8]. Regarding the latter parameter, Li-ion batteries work efficiently when operating between 298 K and 308 K [9–10]. In particular, high-temperature operative conditions involve recognized negative effects on battery performance, mainly in terms of capacity/power fading, self-discharge, and remaining useful life. At the same time, low temperatures affect charge acceptance, actual capacity, and charging/discharging efficiency [11].

For this reason, EVs require proper Battery Thermal Management Systems (BTMSs), the main objective of which is to extend the battery life cycle and optimize performance. In particular, BTMSs must be able to control maximum and minimum temperature values inside the Battery Pack (BP), prevent sudden temperature variation, and avoid battery cells' exhaust gas stagnation [12]. Currently, traditional BTMS classification is based on the medium used for heating/cooling operations such as air, liquid, and solid medium. Every BTMS is characterized by different advantages and limitations to be taken into account on the basis of the operative context. For example, BTMS based on air medium is characterized by different advantages in terms of weight, cost, and size. On the other hand, air has poor thermal properties, and it results less effective in thermal management than liquid-based BTMS [13]. Therefore, the choice and size of BTMSs are mainly based on an evaluation of the amount of heat to be dissipated during EV operations. The amount of heat depends on several factors, such as BP technology,

* Corresponding author.
E-mail address: clemente.capasso@stems.cnr.it (C. Capasso).

https://doi.org/10.1016/j.est.2023.109971
Received 17 July 2023; Received in revised form 13 November 2023; Accepted 2 December 2023
Available online 12 December 2023

layout, materials, and design criteria [14]. Concerning battery heating, the amount of heat generated by a single storage cell is a function of its electrical and thermal behavior. In this case, modelling plays a key role in estimating this behavior, providing input for a suitable BP and BTMS design. However, battery cell behavior is characterized by interconnected electro-thermal physical phenomena during operation. In this regard, the scientific literature proposes different cell models, which mainly differ in complexity, fitting performance, and the focus on specific aspects to be investigated. In particular, the following macro-categories can be identified: Electrochemical Models (*EMs*), Equivalent Circuit Models (*ECMs*), and Machine Learning Models (*MLMs*) [15,16].

EMs, based on complex physics and chemistry theories, aim to predict diffusive electrode phenomena and electrochemical reactions between electrodes and electrolytes. Every single physical phenomenon that takes place in the battery cell is evaluated through partial differential equations [17–19]. For this reason, EMs offer a highly accurate dynamic representation of what happens inside the battery cell. However, EMs require a great amount of computational resources and time to obtain the desired simulation results. This model is therefore mainly used in experimental studies addressing nonlinear battery cell behavior. A typical application based on this kind of model is reported in [20], where an EM, called *P2D*, was combined with a mosaic model in order to describe the transport mechanism between graphite and LPO cathodes of 18,650 cylindrical battery cells. In this case, the EM was validated by performing discharge tests at different C-rates: results fit well with experimental data in terms of the expected phenomenon inside the battery cell. In [21], Schmidt et al. presented a Multi Scale Multi Domain (MSMD) model to evaluate the electro-thermal behavior of a large prismatic battery of 120 Ah. The model is composed of a three-level structure to describe the particles, electrodes, and cell electrical phenomena. An extension of *P2D* Newman's model approach was used to make the multilayer structure of the battery cell homogeneous. The superiority of this modelling strategy was shown by analyzing the effect of high discharging operations on battery cell temperature distribution at different battery cell cooling conditions. MLMs represent an opposite approach that is adopted when the studied phenomenon cannot be conveniently analyzed using simple mathematical equations. Such models use data-driven algorithms to estimate specific cell parameters, such as SoC and SoH, on the basis of indirect experimental measurements. MLMs generally call for initial processing, which is particularly demanding in terms of both time and computational effort [22–24]. Their development involves three steps: data preprocessing, training and validation. These models are therefore mainly used for near real-time nonlinear evaluations, which can be performed rapidly and accurately after initial processing. However, MLMs generally require a lot of experimental data, since their fitting performance decreases when dealing with unexpected behaviors that were not previously considered in the training datasets. In this regard, Sheng et al. [25] have trained an MLM to estimate the SoC for a $LiFePO_4$ battery cell. In this case, preprocessing of experimental data was carried out using the Fuzzy Least Squares Support (LSS) method to reduce noise-sensitive issues. Results suggest that Fuzzy LSS allows higher estimation accuracy and better noise immunity with respect to the ANN method. Of the models described, ECMs represent a good trade-off in terms of fitting performance and computational effort. These models are based on electrical equivalent circuits that simulate the electric behavior of battery cells under different operating conditions. The most frequently used ECM is the *Rint model*, which only describes battery cell voltage drop during operation, and the *Thevenin Model (TM)* and *Dual Polarization Model (DPM)*, which describe the dynamic behavior of electrical battery cells [26,27]. In this regard, Zhang et al. [28], analyzed *TM* and *DPM* accuracy by comparing experimental and simulation results from a *1C* discharging test on a *18,650* cylindrical battery cell (2350 mAh). Although the fitting performance of the *DPM* was better than that of the *TM*, the improvement in accuracy was almost negligible and did not justify the greater computational effort.

The electrical behavior of a battery cell can also be directly linked to its thermal behavior. Electrical parameters and chemical reactions in cathodes are the main factors responsible for heat generation inside battery cells. Bernardi et al. [29–30] formulated an equation to estimate the generation of reversible and irreversible heat, related to entropic and Joule effects respectively. Evaluations are generally used as inputs for storage cell thermal models, which focus on describing the thermal behavior of cells.

Thermal models are generally divided into two categories: *Physical models (PMs)* and *Lumped models (LMs)* [31]. *PMs* describe physical phenomena occurring inside and outside the storage cell. Thermal models use general expressions that combine heat rate generation and temperature distribution terms. PMs assume that battery cells can be evaluated through thermal parameters distributed over one, two or three dimensions. In [32], Ynui et al. developed two *PMs* in order to compare simulation and experimental temperature distribution results in different case studies. In particular, a cylindrical and a prismatic battery cell were respectively modelled through two- and three-dimensional *PMs*. As a case study, the transient temperature profile of a battery cell core was monitored during a discharging current. For both battery cells, the simulated temperature distribution fit experimental results very well, suggesting the great accuracy of this model. For this reason, *PMs* are mainly used in CFD analysis. However, despite their accuracy, *PMs* require great computational effort in modelling and simulation.

LMs are useful in describing the thermal behavior of storage cells using the circuit analogy for cell thermal physics. For example, a heat capacitor inside a thermal circuit can be used to simulate the battery cell's ability to store thermal energy. This makes it possible to achieve a good compromise between model accuracy and computational effort [33,34]. In [35], Lin et al. developed a *LM* to describe the thermal behavior of a cylindrical cell. In particular, the proposed *LM* adopted only four parameters to estimate the transient thermal behavior of the cells. Two thermal capacitors were used to model the core and the surface of the cell, and two thermal resistances were used to simulate heat exchange. This model was further simplified in [36], where Forgez et al. developed a reduced *LM* based on the assumption that the core and surface work at the same operating temperature. The *LM* was validated through charging/discharging pulses, which highlighted the good accuracy of the proposed model in predicting temperature behavior. Table 1 provides an overview of the main battery cell model typologies used in the literature.

Starting from the **above** considerations, complex systems such as BPs require a transversal modelling strategy based on *multi-domain* modelling approaches [37]. Multi-domain modelling strategies are based on interconnections and multidisciplinary relations among all the different physics domains pertaining to the system being analyzed, as shown in Fig. 1.

This approach generally yields more accurate results and requires a lower simulation effort than traditional sequential modelling strategies. It involves *Object-Oriented*, *Non-causal* and *Narrative modelling*, which make modelling intuitive and simple for users. The user can model the system by interfacing different domain classes without using complex equations [38]. The Simulink toolbox *Simscape* and *Modelica* are two examples of software tools supporting this kind of modelling strategy. As reported above, a vehicle BP can be considered a complex system in which electrical, control and mechanical domains operate in synergy: as the temperature of BP cells varies during electrical operations, the BMS interfaces with sensors to monitor such variations and controls the cooling system to dissipate any excess heat. In [39], Bordes et al. developed a collaborative platform for the integration of different simulation models. In this work, the open Functional Mock-up Interface (FMI) was used for interfacing a power train and a battery controller software models. In particular, the two models were developed in Modelica and Simulink frameworks and converted into Functional Mock-up Units (FMUs) to be implemented in the Jupiter Notebook

Table 1
An overview of the main electrical and thermal battery models.

Macrocategory	Key elements	Battery chemistry	Ref.
EM	Adaptive Partial Differential Equation (PDE) model for SoC and SoH estimation.	General considerations not dependent on battery chemistry.	[17]
	Non-Linear Dynamic SPICE math model for DC nonlinear battery behavior estimation.	Ni-H_2	[18]
	Pseudo 2-Dimensional (P2D) model for temperature prediction.	Cylindrical 5 Ah NMC/Si-Graphite battery.	[19]
	P2D model for terminal voltage estimation.	Cylindrical 1.05 Ah $LiFePO_4$ battery cell.	[20]
	Extended P2D Newman model for the estimation of battery cell temperature distribution.	NCA/LCO blend cathode 120 Ah prismatic battery cell.	[21]
MLM	ANN model for SoC and SoH estimation of aged battery cell.	Pouch 15 Ah NMC.	[22]
	Input time-delayed NN model for SoC and SoH estimation	20 Ah $LiFePO_4$ prismatic battery cell	[23]
	Implementation of Quantum Particle Swarm Optimization ML technique for the evaluation of remaining battery cell capacity.	Cylindrical 3.45 Ah Lithium polymer of	[24]
	Fuzzy Least Square Support Machine Vector model for SoC estimation.	50 Ah $LiFePO_4$ prismatic battery cell	[25]
ECM	Rint, Thevenin, and Dual Polarization Model for testing a new battery cell parameterization technique	Cylindrical 2.9 Ah Lithium polymer battery cell.	[26]
	Dual Polarization Model for the estimation of SoC vs OCV behavior.	2.5 Ah $LiFePO_4$ and Lead-Acid battery cells	[27]
	Thevenin and Dual Polarization model for battery cell terminal voltage prediction.	18,650 Cylindrical 2.35 Ah lithium polymer cell.	[28]
PM	Time-dependent simulation code for battery cells temperature distribution estimation.	1.8 Ah Cylindrical and 9 Ah prismatic Lithium polymer battery cells.	[32]
LM	4 States LM for testing a new parameters' identification methodology.	2.35 Ah Cylindrical $LiFePO_4$ battery cell.	[33]
	3 States LM for BP module temperature estimation.	3.8 Ah cylindrical $LiFePO_4$ battery cell.	[34]
	2 state LM for battery cell temperature estimation.	3.8 Ah cylindrical $LiFePO_4$ battery cell.	[35]
	2 state LM for temperature estimation.	2.35 Ah Cylindrical $LiFePO_4$/Graphite battery cell.	[36]

scripting environment. The analysis of the described simulation platform was carried out with a specific focus on battery charging procedures. On the other hand, the approach of Byung et al. [40] was based on developing the BP model in one simulation environment. In particular, an electro-thermal multidomain model of a BP equipped with liquid based BTMS was developed in Simscape Simulink environment. The cooling efficiency of two different BTMS solutions was investigated through numerical and experimental activities, comparing the cold plates' thermal resistance trends at different C-Rate discharging values. In [41], Smith et al. used a multidomain model in order to help the BP design activities. The cylindrical cells which compose the BP were modelled using a Thevenin ECM and PM for the estimation of its electrical and thermal behavior. In addition, a lumped parameter model was used to evaluate the BP Module thermal distribution during operations.

However, the most popular multi-domain modelling strategy for BPs involves the use of Computational Fluid Dynamics (CFD) software [42]. For example, Shung-bo et al. improved the air-cooling BTMS by

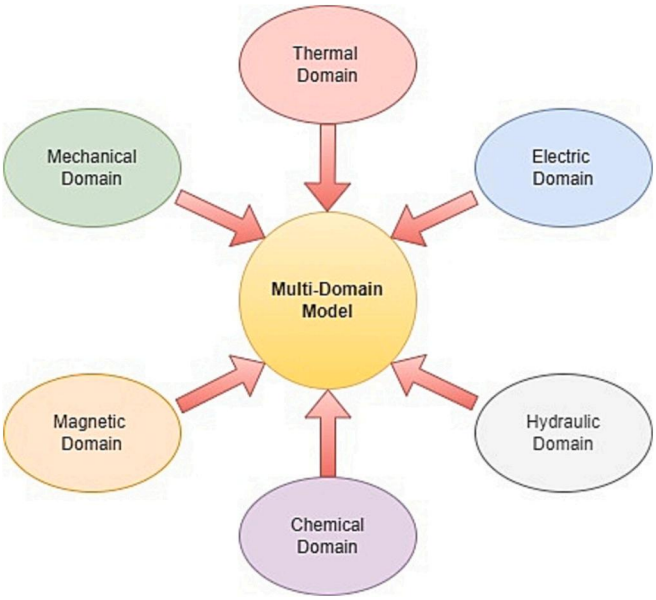

Fig. 1. Multi-domain modelling.

redesigning the array of outlets along the normal flow stream. The Ansys Fluent CFD method was used to calculate temperatures and the flow field. In [43], Okaeme et al. presented a systematic multistage modelling approach for designing and optimizing the BTMS for hybrid trucks. Despite its accuracy, the application of CFD to the study of BPs requires long simulation times and great computational effort due to the complexity of solutions for the Navier-Stokes equations [44]. This approach can therefore be considered useful for detailed analysis of single systems with a given configuration. Within this context, this work presents a multi-domain modelling approach for the design and sizing of new energy storage system (ESS) configurations for EVs, taking into account experimental electro-thermal data at a single cell level for a given BP layout and thermal management system. Compared to traditional methods proposed in the scientific literature, the novelty of the proposed approach lies in its flexibility during design activities and the good fitting performance obtained by linking geometrical and experimentally validated lumped parameter models [45]. This allows reliable, easy, and fast evaluation of the electro-thermal behavior of EV BP in terms of temperature distribution and hot spots while operating under different conditions.

The rest of the paper is organized as follows. The case study and BP modelling operations are described step-by-step in Section 2. Experimental tests performed for battery cell model parameter identification and validation are detailed in Section 3. Lastly, the main findings are presented and discussed in Section 4.

2. The case study and modelling

The evaluations reported in this paper are based on a vehicle BP composed of EIG ePLB C020 lithium cells (Fig. 2). In particular, the considered cell cathode is based on Nickel-Manganese-Cobalt compounds, distributed in 4:4:2 proportion. The anode is composed of graphite type material, improved with vapor grown carbon fibers (VGCF) for the optimization of electrical conductivity. The electrolyte is based on BASF (LP50) containing 1 M LiPF6 in 1:1 volume ratio mix of ethylene carbonate (EC) and dimethyl carbonate (DMC). The investigated cells have higher storage capacity than the LiNMC cells with 1:1:1 composition [46,47] and they are widely used in the automotive sector thanks to their good performance in terms of energy/power density and charging/discharging efficiency [48]. A picture of the considered cell and its main characteristics are reported respectively in Fig. 2 and

Fig. 2. The Li(NiCoMn)O_2 cell and its characteristics.

Table 2
Main characteristics of the Li[NiCoMn]O_2 cell.

Cathode chemistry	NMC (4:4:2)
Electrolyte chemistry	BASF (LP50) mixed with EC and DMC (1:1)
Nominal voltage	3.6 V
Nominal capacity	20.0 Ah
Specific energy	180 Wh/kg
Maximum charge voltage	4.2 V
Maximum charge current	1C
Lower voltage limit	2.5 V
Maximum discharge current	5C
Maximum peak discharge current	10C

Table 2.

It is important to develop a suitable electro-thermal model for the above cell to enable the design and testing of appropriate cooling systems for BPs based on this technology. NMC battery cells work properly in a certain temperature range. Outside this range, battery cell performance is poor and there is a fire hazard due to reduced chemical stability.

The proposed methodology for BP modelling is based on a bottom-up approach, starting from the single cell level up to evaluation of the whole BP multidomain model. The workflow of this methodology is summarized in Fig. 3.

At the single-cell level, electro-thermal lumped parameter models based on the *Thevenin Model* and the *One-State Lumped Model* were chosen to achieve good accuracy with low computational effort. Heat generation was evaluated based on a few simplifying hypotheses. As for the *Bernardi* equation, only irreversible losses due to the *Joule effect* were considered. In addition, the battery cell core and surface were considered to have the same temperature and the flow of current inside the battery cell was considered to be uniform [49].

Considering the thermal behavior of this kind of battery cell, the above assumptions are reasonable. The thickness of a pouch cell is such that the difference between core and surface temperatures is negligible. Starting from these considerations, a *Single-cell model* was used to simulate heat exchange between the battery cell and the environment. A *Two-Cell Interaction* model was developed to study thermal interactions among battery cells. Said models were subsequently integrated into the *BP numerical model* and linked to the Geometric BP model in order to evaluate the effects of BP layout on the thermal behavior of individual cells. The following is a detailed description of the modelling approach.

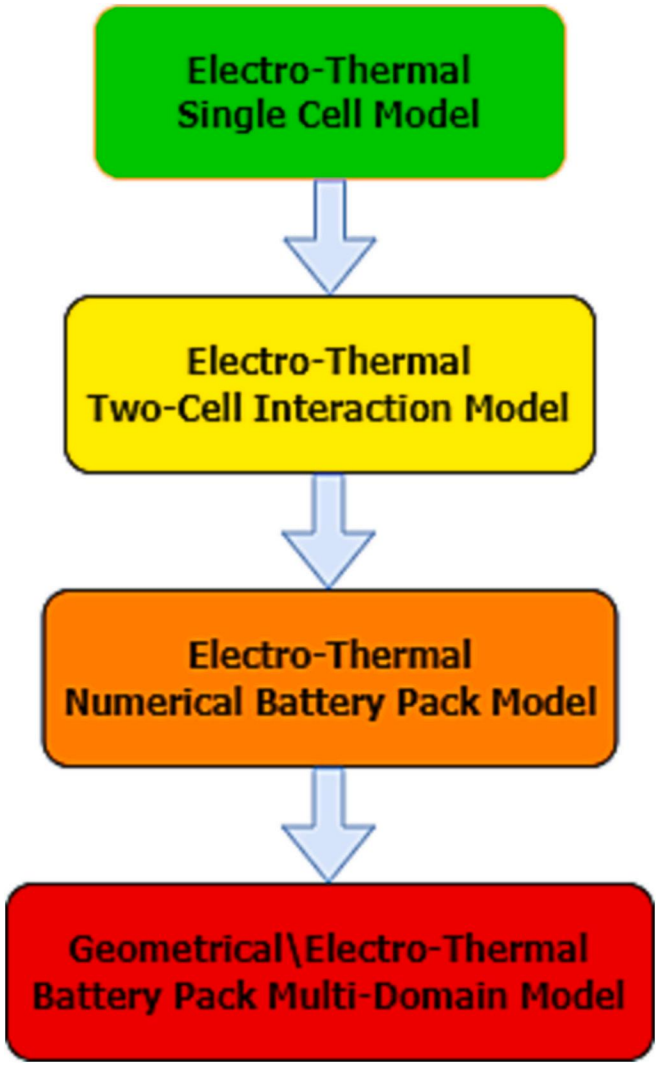

Fig. 3. Battery pack modelling workflow.

2.1. The electro-thermal single cell model

The developed electro-thermal *single cell model* comprises the *Thevenin Equivalent Circuit Model*, representing the electrical behavior of the battery cell, and the *One-State Lumped Thermal Model*, representing the thermal behavior of the battery cell. The electrothermal model scheme is shown in Fig. 4.

In particular, for the electric part, the voltage generator simulates the *Open Circuit Voltage* (*OCV*), whereas Ohmic resistance (*Rint*) is used to estimate voltage drop within the battery cell and Joule Losses. An *RC* branch is used to describe the transient behavior of the cell during operating cycles. In the thermal part, a *Thermal Capacitor* simulates the battery cell thermal behavior estimating its Temperature value. The *Thermal Capacitor* is linked to a *Constant Temperature Source*, by means of a *Convective Resistance* (R_{amb}), to simulate the heat exchange between battery cell and environment. The battery cell SoC is estimated through the *Coulomb Counting Method* after setting the initial capacity value at the beginning of the simulation [50]. The temperature value is obtained using the *Thermal Model*. The *State of Health* is determined in the *Electrical Parameter Estimation block* through linear interpolation (Eq. (1)):

$$SoH = \frac{R_e - R}{R_e - R_n} \tag{1}$$

where *Re* and *Rn* are aged and brand-new internal resistance values

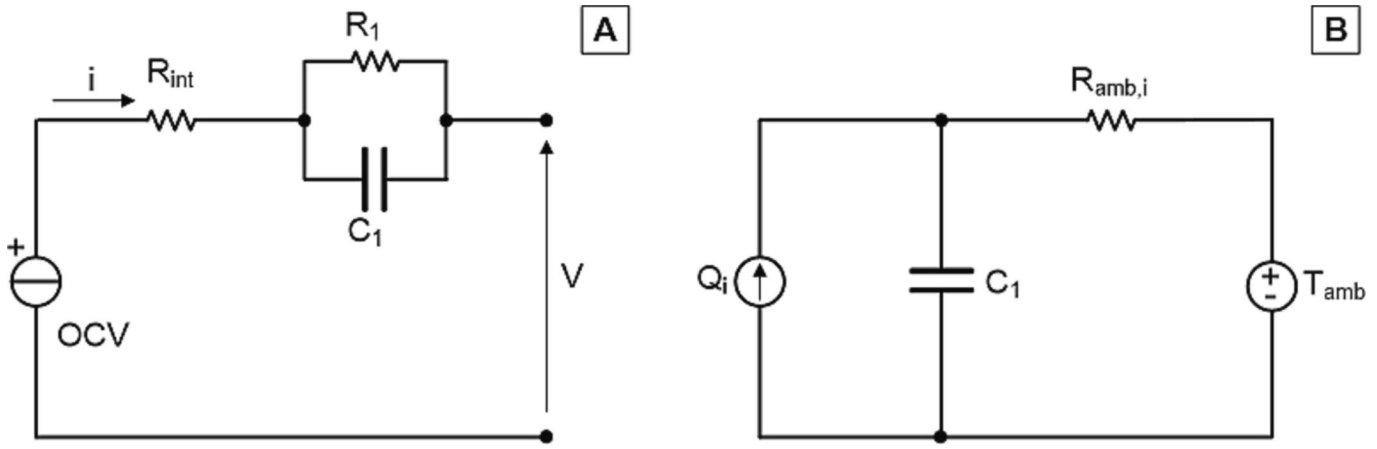

Fig. 4. The Thevenin Equivalent Electric Circuit Model (a), and the One-State Lumped Thermal Model (b).

respectively, and R is the instantaneous resistance. *Re* and *Rn* values are based on experimental results [51,52].

2.2. Two-cell interaction model

In this study, a two-cell interaction model was developed to analyze how cells inside the BP influence each other from a thermal perspective. This model helps improve the thermal circuit between the batteries by simulating the behavior of the environment surrounding the cells. The air surrounding the battery cells influences cooling and heating during operation. Battery cells exchange thermal energy with the surrounding air, modifying its temperature. Increases in air temperature affect heat exchange with the battery cells, which cannot be cooled effectively. To simulate this behavior, the air between the cells is modelled as a thermal mass that can store and release thermal energy. The electrical and thermal scheme of the *Matlab-Simulink* model is reported in Fig. 5.

In the figure above, the two cells are electrically connected in series (a). In thermal terms, *convective resistances* connect every cell in parallel with the air between cells and the air on the other side of the battery cells. The ambient temperature around the free battery cell side is modelled as a *constant temperature generators*, assuming that the huge quantity of air on the outside is not affected by changes in battery cell temperature. The temperature of the air between the cells is affected by temperature variations in both battery cells. To estimate the volume of air between the two battery cells, the distance between them and the air density must be estimated. The first parameter can easily be set at the start of the simulation. Air density depends on several parameters such as ambient pressure, temperature and altitude. This variability is overcome by assuming that the initial air density value remains constant throughout the simulation. This is a reasonable assumption, considering that the ambient pressure does not vary during battery cell operation and that variations in air density due to rising battery cell temperatures during operation is negligible. The air density can therefore be considered constant throughout the simulation, and the mass between the cells can be easily calculated using the density formula. Setting the cell position before simulation, the volume is determined, and the mass can be calculated as follows:

$$mass = \rho^{*}V. \tag{2}$$

where ρ is density (kg/m^3) and V is volume (m^3).

This model is crucial to the development of the BP model. This numerical model for the behavior of air can be used to simulate the development of temperature hotspots in the BP during operation. The air surrounding battery cells located in the middle of the BP will be hotter than that surrounding the batteries at the two ends of the BP. This allows a more accurate estimation of temperature distribution within the BP.

2.3. The air-cooling system model

The *BTMS* can improve the temperature distribution of BPs by keeping temperature differences among battery cells as low as possible.

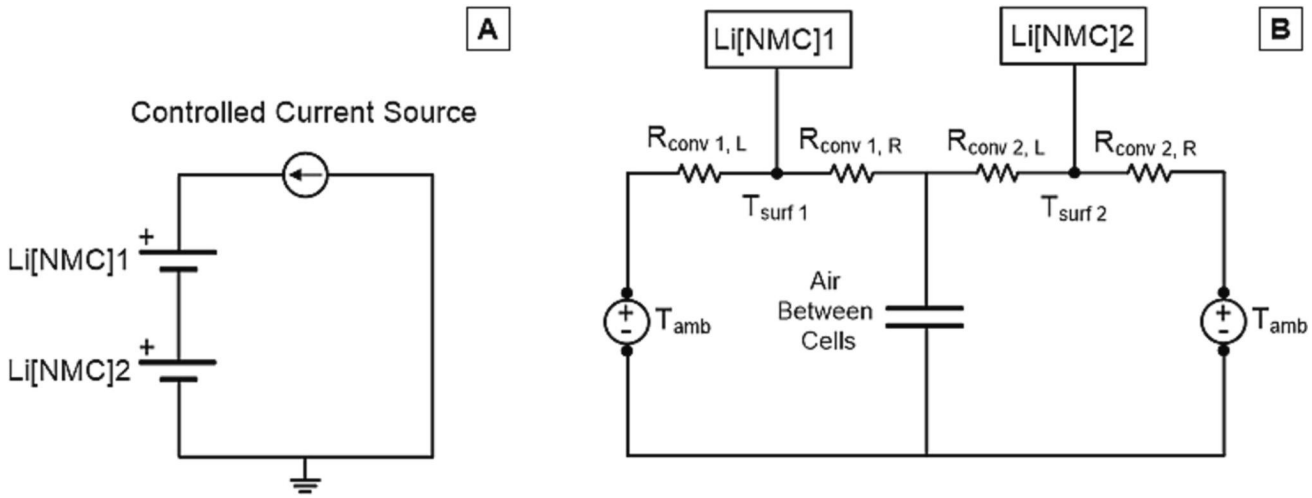

Fig. 5. Two-cell interaction model: electric (a) and thermal (b) scheme.

The *BP* model was improved by implementing a *BTMS* in order to compare the effectiveness of the cooling system on the layout created. In particular, the implemented *BTMS* is based on an air-cooling strategy. Starting from a *Two-cell interaction model*, the model was developed on the geometric assumption that the space between the two battery cells is like a smooth pipe, as shown in Fig. 6, having diameter and length respectively equal battery cell width and length.

From this perspective, heat exchange between the lithium cells and air can be studied as internal forced-convection heat transfer. Further assumptions on fluid motion must be made in order to simplify the system model. In particular, the coolant medium is considered an Ideal Gas, and the flow stream is studied as a unidirectional flow moving in the direction of battery cell major axis. In addition, during the simulation the Reynolds number at the transition from laminar to turbulent motion is set at 10000. The above assumptions are justified by the small size of the system considered [53]. From a thermodynamic perspective, the temperature of the cooling medium along the pipe is considered exponential in order to evaluate heat exchange between air and battery cells using the following Eq. (3):

$$Q_{conv} = |\dot{m}|c_p(T_W - T_{in})\left(1 - exp\left(-\frac{h\,A_s}{|\dot{m}|c_p}\right)\right) \tag{3}$$

where $\dot{m}$ and c_p respectively represent the average air mass flow inside the pipe and the specific heat at the average temperature within the duct. The parameters A_s and T_{in} refer to the heat transfer contact area between the air and the lithium cells and the intake temperature of the cooling medium respectively. The h value is determined considering the mean flow direction value and is calculated through Eq. (4):

$$h = Nu\,\frac{k}{D_h} \tag{4}$$

where *Nu* is the *Nusselt* number, k is the average thermal conductivity of the cooling medium and D_h is the pipe's hydraulic diameter. It is assumed that the air mass flow is provided by the fan to the system instantly and that the fan is a constant source with no inertia. In addition, *BTMS* is based on hysteresis control. The fan turns on when one of the battery cells reaches an operative temperature five degrees higher than its initial simulation value and turns off when the hottest *BP* cell has an operative temperature one degree below the control limit temperature value.

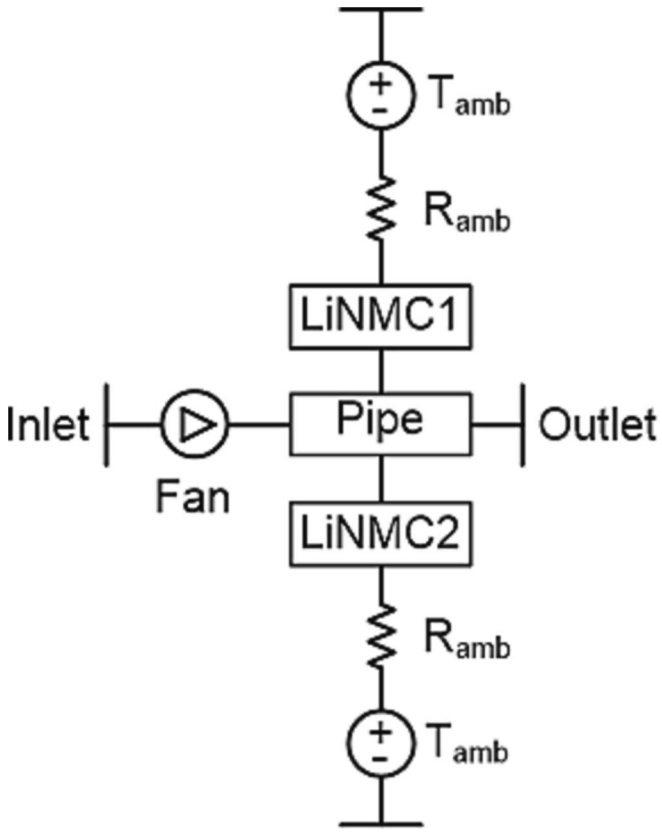

Fig. 6. The air-cooling scheme.

2.4. The battery pack numerical model

The BP model was developed on the basis of a *Two-cell Interaction model*. In particular, the model simulates the behavior of every single cell in the BP and the environment that surrounds them. In addition, the implementation of an *Air-Cooling System model* enables simulation of the air-mass flow between the battery cells as well as electro-thermal interaction between the BP and the air-cooling system. When the cooling system is off, the BP thermal circuit links the battery cells and the air that surrounds them, as shown in Fig. 9. Depending on its placement, each battery cell is linked to two air masses that simulate the air between the previous and the subsequent battery cell in the string. At the same time, the battery cell is linked to two other air masses that simulate the air between the different rows. The first and last battery cell in each string is linked to a *Constant Temperature generator* in order to simulate the huge air mass representing the environment surrounding the BP.

When the cooling system is switched on, the fan forces the air mass to move between the battery cells. Each *NMC* cell builds up two rectangular ducts with the previous and next one of the same strings. Considering the above, each *BP* string contains *n-1* rectangular ducts.

The ducts of each string are linked in order to cross the *BP* transversally. Each duct is linked to the next one of the following strings crossing the *BP* in *a* transversal direction, as shown in Fig. 7.

In each duct, the air flow stream is a fraction of the total mass flow provided by the fan, depending on the position of the pipe in the layout. In this configuration, all the rectangular pipes start from the same inlet and are divided during the heat exchange with battery cells. At the end of the pipe, the outlet is set to ambient parameters. In addition, the first and last lithium cells of the same string have only one side in contact with the forced cooling medium: the other side is linked to a thermal mass that simulates steady air motion between the battery cells and the walls of the *BP*.

2.5. The battery pack geometric model

A Battery Electric Vehicle's energy storage system can be seen as a complex system in structural terms. It consists of several battery cells optimally positioned to save space in the EV and to improve heat exchange between the battery cells and the cooling system. The design of this system requires the use of the CAD modelling methodology, which supports development and review activities in the design of complex systems. Furthermore, the model must be modified without losing the main *functional relationships* among the model's main features in order to allow different system configurations without having to redesign the system itself. In this context, a *Top-Down* approach was used in geometric modelling. This approach is typically used in modelling the virtual assembly of complex systems. Design activities focus on overall assembly and the functional parts, whereas secondary parts are modelled later. This kind of approach places functional design requirements at a higher level. In this way, critical design information is transferred to all related subsystems. The BP model was developed in the *SolidWorks* environment. It is a *Computer-Aided Drafting* software used in 3D parametric virtual modelling. The creation of a BP geometric model starts with the study of BP morphology. BP geometric analysis is followed by the identification of the key geometric characteristics defining the model's *skeleton*. The skeleton is the reference structure of the model. The BP skeleton (Fig. 8) is the basic layout that shares critical

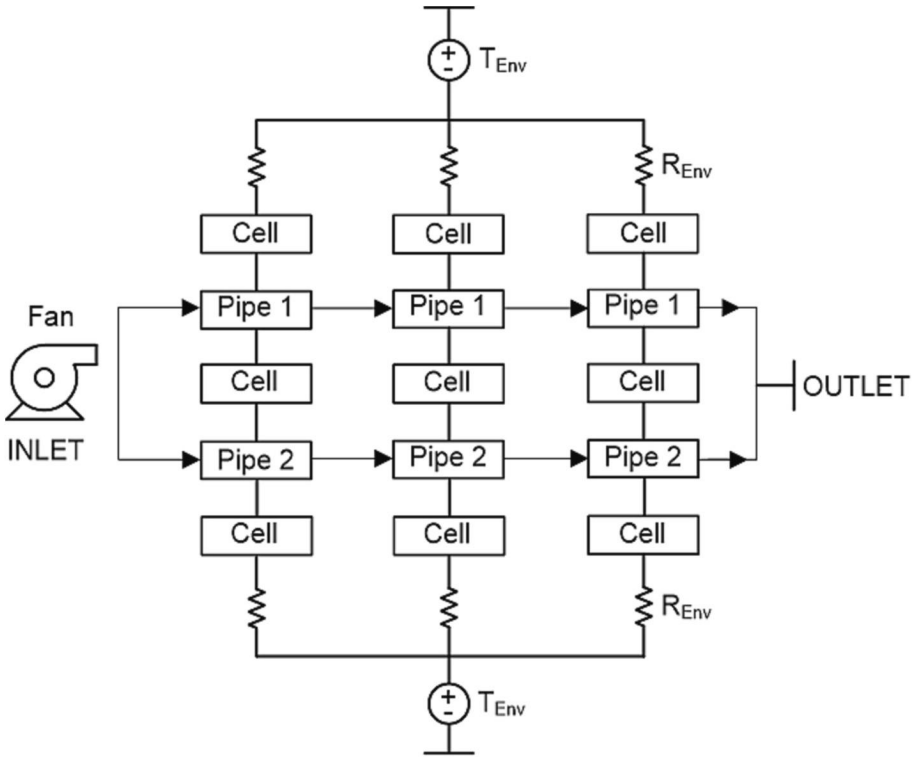

Fig. 7. Battery pack with air cooling scheme.

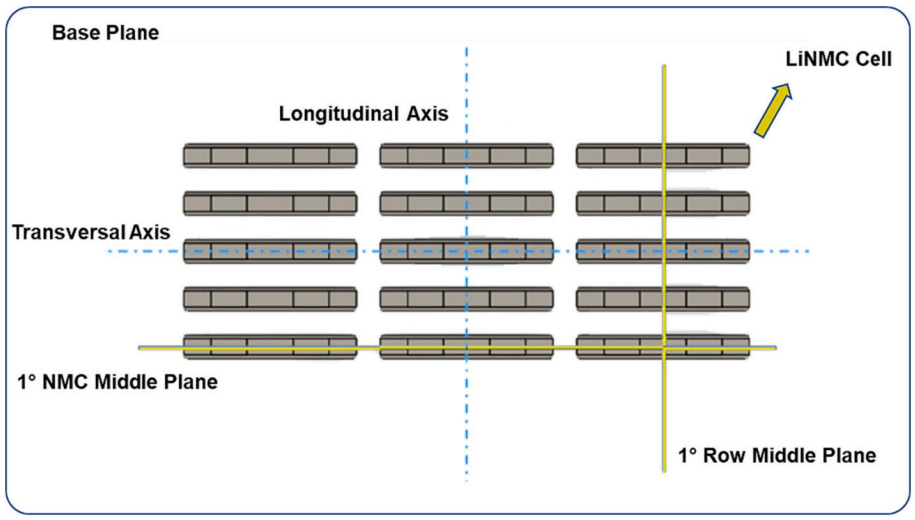

Fig. 8. Battery pack skeleton scheme.

information with the assembled elements, creating a parent-child relationship with them.

Fig. 8 shows the main geometric features of the *BP*. The BP skeleton consists of the *1st row Middle Plane*, the *1st NMC Midplane*, the *Longitudinal* and *Transversal* axes and the *Base Plane*. These geometrical features are essential in defining the BP configuration and layout. The first reference is *1st row Middle Plane*. This geometric feature runs along the middle of every single cell in the 1st row, and defines the transversal distance between the first string and the center of the BP. The second reference feature is the *1st NMC Middle plane*, which contains the first cell of every single row. This reference feature fixes the longitudinal distance of the first NMC in the rows and the position of the first NMC in the first string. The *Longitudinal* and *Transversal* axes divide the BP into four symmetrical parts. These reference features provide modelling instructions for the design of the BP layout. Lastly, the Base Plane describes the geometric boundaries of the inner part of the BP and limits the area where battery cells are positioned. All *skeleton references* are parameterized, creating global variables that are linked to the main geometric features of the BP. Global variables are reported in Table 3.

Global variables are integrated into the SolidWorks environment using Eqs. (3) and (4). The equations describe the position of the center of the first cell in the first string. The equations are as follows:

$$\frac{d}{2}+(d+t)*\left(\frac{N_s}{2}-1\right)+\frac{t}{2} \tag{3}$$

Table 3
Variables used in the geometric model.

Global variables	Description
W	NMC width
L	NMC length
T	NMC thickness
S	Transversal distance between cells
D	Longitudinal distance between cells
Np	Rows in parallel
Ns	Cells in series

$$\frac{s}{2}+(l+s)*\left(\frac{N_p}{2}-1\right)+\frac{l}{2} \tag{4}$$

Eq. (3) describes the center of the first battery cell in the first-string position for the reference transversal axis, whereas Eq. (4) describes the same center for the reference longitudinal axis. BP modelling starts with NMC modelling. The NMC design is shown in Fig. 9.

The cell is positioned sideways, with the longest dimension in contact with the base of the *BP*. The battery cell model is repeated for the number of cells in the row, and every row is repeated several times to obtain the BP model. The geometric model is obtained by repeating the first battery cell model N_s times along the longitudinal axis in order to make up the first string of the BP. The first string is repeated N_p times long the direction of the transversal axis to obtain a BP composed of the pre-established number of battery cells. By changing global variable values, the model can be customized.

3. Experimental measurement campaign

3.1. Experimental setup

A specific laboratory setup was used to fully characterize lithium cells operating under different electric and thermal conditions. The functional scheme of the laboratory setup is reported in Fig. 10.

All tests were performed at constant ambient temperature values. These conditions were achieved using an *ACS Discovery* Climate Chamber with an internal volume of 340 L. The chamber can be controlled in terms of temperature and humidity within the ranges 238 to 453 K and 10 % to 98 % respectively. The temperature of the tested storage cell/module was recorded by PT 100 probes connected directly to the cell surface. Cell/module cycling operations were performed through controlled DC power suppliers and DC electronic loads working together in order to run charging/discharging current/voltage/power profiles. These profiles can be set by the user through suitable software interfaces developed in the *National Instruments – Labview* Environment. A *LEM HAL-50 S* current transducer was used to measure the current, whereas battery voltage was determined by connecting the cell poles directly to the voltage acquisition module. A National Instruments Compact Daq NI9188 equipped with voltage, current and temperature acquisition modules was used for data acquisition.

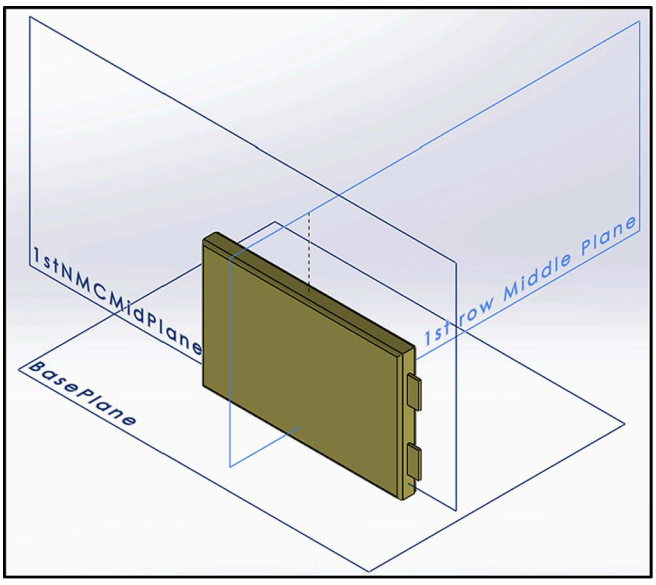

Fig. 9. NMC battery cell in the battery pack.

3.2. Experimental tests

The experimental characterization and parameterization tests focused on two NMC cells with different *State of Health*. Laboratory tests were performed first on an end-of-life battery cell and then repeated on a brand-new battery cell. The first test was a *Capacity* Test, which evaluates the actual capacity of the considered battery cells under different constant current discharging operations. Prior to this test, each battery cell was recharged through a CC/CV charging operation with a maximum charging rate of 0.2 C. The test was performed at a fixed ambient temperature of 298 K. The results for the aged cell are shown in Fig. 11.

As shown above, the aged cell reached an actual capacity value of about 16 Ah at 0.25C. Although the discharging current was very low, the resulting capacity value corresponds to the 80 % of the cell rated capacity. The low state of health of the cell was confirmed by the 1C discharging rate test, where the cell showed an actual capacity of 1.2 Ah, corresponding to 6 % of the rated cell capacity. This cell was therefore adopted as the reference aged cell with SoH = 0 %.

The 1C Capacity test was repeated on the brand-new cell, and results are shown in Fig. 12.

The tested cell yielded an actual capacity of 24 Ah, corresponding to 120 % of its rated capacity; its *SoH* was assumed to be equal to 100 %.

Electro-thermal lumped models for both cells were parametrized from an electrical and thermal perspective using the *Hybrid Pulse Power Characterization* and *Thermal Relaxation* tests respectively. The *HPPC* test is typically used to measure the dynamic electrical behavior of energy storage systems from the standpoint of either module or single cell. The test is characterized by several high discharging/charging current pulses at different *SoC* steps, from 100 % to 15 % [54].

Fig. 13 shows the *HPPC* results for the brand new NMC cell.

Focusing on a single *HPPC* step, the current profile shows discharging and charging pulses at *1C* with a duration of 10 s. After each pulse, the battery cell rested for about 40 s. At the end of each step, the battery cell *SoC* was decreased by applying a *0.25C* discharging current for about 24 min. This strategy was adopted to decrease the *SoC* value by about 10 %; the electrical load step was repeated after a resting period of about 7200 s. Every step was repeated until the cell *SoC* reached the 20 % value. After this, the last *HPPC* step was repeated, decreasing the *SoC* by only 5 % in order to avoid over-discharging the battery cell. The same test was performed on the aged cell, taking into account different 1C pulses and compensation phase durations on the basis of capacity test results. The relationship between electrical parameters and operative temperature was obtained by performing *HPPC* at different ambient temperatures of 298, 303 and 308 K. Fig. 14 shows the *Thermal Relaxation* test for the brand new NMC cell.

The main aim of the latter test is to analyze how battery cells store and release thermal energy during operation The test is composed of two main parts. The battery cell is first overheated by several *1C* discharging/charging pulses for 3 h. During this time, the cell temperature increases until it reaches thermodynamic equilibrium with the environment. When equilibrium is reached, the electrical load is removed and the battery cell rests for 7200 s in order to reach ambient temperature. The above tests were used for electrothermal model parameterization. In particular, parameterization was performed using the Matlab/Simulink *Parameter Estimator Toolbox*. The *HPPC* test yields

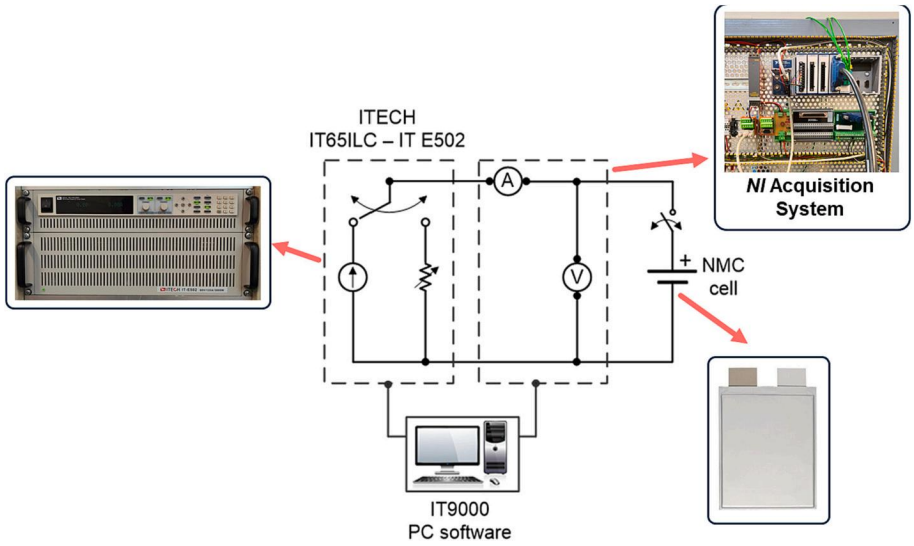

Fig. 10. Functional scheme of the laboratory setup for electro-thermal testing.

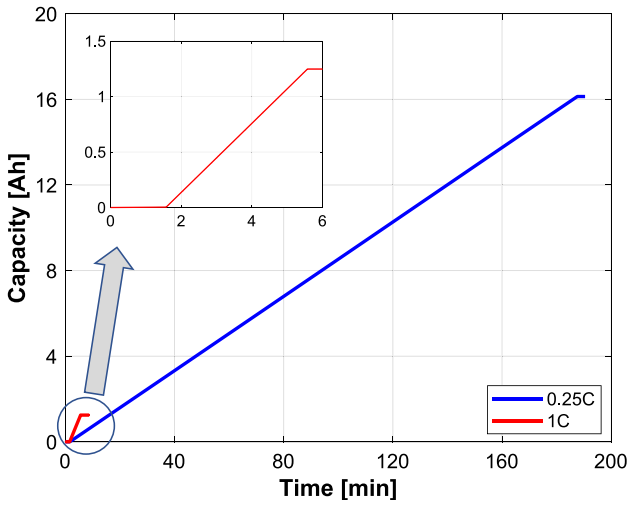

Fig. 11. Comparison between aged capacity and the 0.2-1C discharging test.

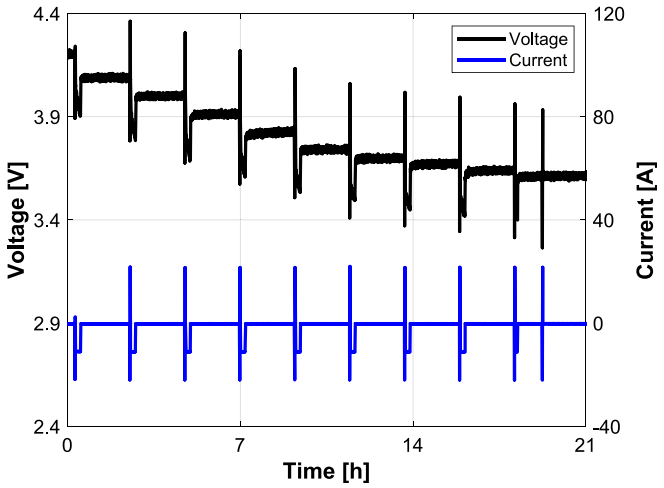

Fig. 13. HPPC test performed on the brand new cell.

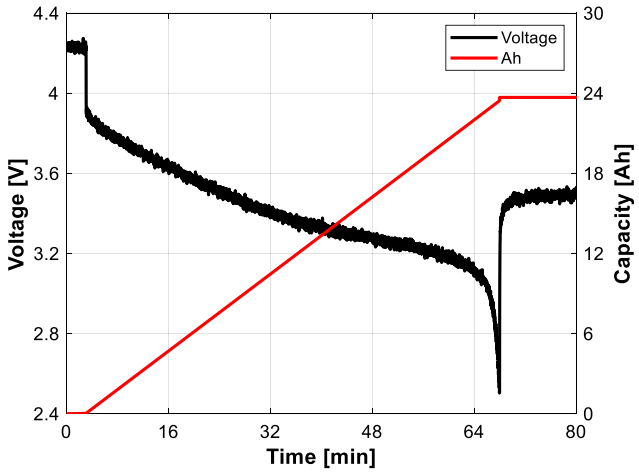

Fig. 12. Capacity versus voltage for the brand new NMC cell during the capacity test.

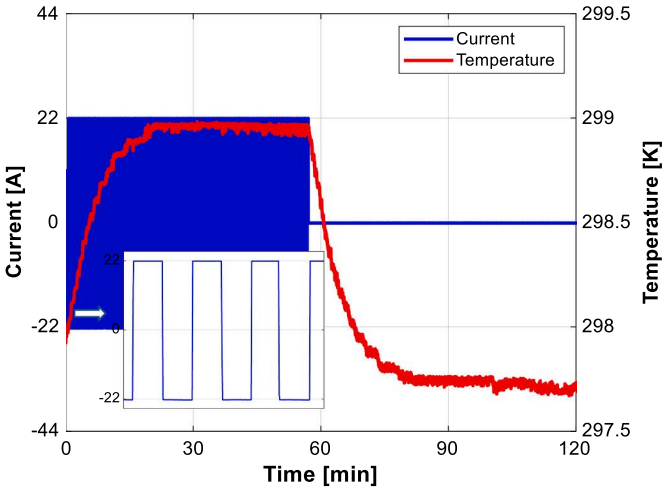

Fig. 14. Thermal test performed on the brand-new cell.

the following electrical parameters: Open Circuit Voltage (OCV), ohmic and polarization resistances and polarization capacity. These parameters were obtained for both the aged and the brand new battery cell. The value of electrical parameters was calculated using Eq. (1) in the *MatLab* workspace before running the simulation. The Thermal Relaxation test is used to estimate the *average convective heat coefficient* (W/m^2) and *thermal capacity* (J/K).

3.3. Validation tests

The parameterized model was validated to assess its performance and accuracy. HPPC at 298 K was chosen to evaluate simulated storage cell behavior. The parameters monitored during the simulation were *terminal Voltage* and *Temperature*, which respectively consist of the output of the electrical equivalent circuit and lumped parameters thermal models implemented in Matlab/Simulink environment and described in Section 2.1. The input provided to the *single-cell model* was the current profile measured in the experimental test. In this test the boundary condition is the same as that of the performed experimental *HPPC*: initial *SoC* and *SoH* values were 100 %, and the initial battery cell temperature was the same as the ambient temperature. Simulation results were subsequently compared to experimental ones (Fig. 15).

Fig. 15 compares simulated *HPPC* voltage (a) and temperature (b) results with experimental results in order to highlight fitting performance. The battery cell's dynamic electrical behavior was well predicted, and the simulated temperature profile trend is very near to the experimental one. The error between simulated and experimental trends is shown in Fig. 16.

As shown in Fig. 16, the voltage and temperature residuals between simulated and experimental trends are negligible. In particular, the simulated voltage error remains in the range of about ±0.3 V, whereas the simulated temperature maximum error is below 0.6 K. These results suggest that the developed *single-cell model* can simulate the electro-thermal behavior of battery cells reliably and accurately.

4. Results and discussion

In this study, two different *BP* layouts were considered in order to highlight the benefits of the proposed methodology in analyzing the thermal behavior of BPs. In determining the best layout from a thermal perspective, *BTMS* was considered operative and thermal distribution during its operation was evaluated.

4.1. Simulation tests

In the present case study, the *BP* consisted of 15 battery cells. A greater number of cells can obviously be analyzed by extending the considerations reported for this particular battery module. From a geometric standpoint, two different layouts were considered, taking into account variations in *layout configuration*. This parameter describes how lithium cells are arranged inside the *BP* for a given battery cell position. The considered layouts are shown in Table 4.

The resulting cell layouts are shown in Fig. 17.

With reference to Fig. 17, the first configuration (A) is composed of 3 rows of 5 cells, whereas the second configuration (B) is composed of 5 rows of 3 cells. The two layout solutions were obtained by setting the distance between cells along the same row to 3 mm and between rows to 20 mm.

As for numerical simulations, the same initial conditions were set for all tests (i.e. ambient temperature and air density values were 298 K and 1.16 kg/m^3 respectively). In the simple hysteresis strategy adopted for cooling system control, the fan is activated when the hottest cell surface temperature in the *BP* is greater than 303 K and is deactivated below 302 K. The 11 g/s total air mass flow moved by the fan is considered to be equally divided among the rectangular ducts of the *BP* layout. Considering this air mass flow, the Reynolds number within the rectangular ducts reaches 8570. This value has been obtained through the following Eq. (5).

$$Re = \frac{w_{avg} * D_h}{\nu} \tag{5}$$

where w_{avg} is the air average velocity in the duct, D_h is the square duct hydraulic diameter and ν is the cinematic viscosity. The average air velocity is derived by the air mass flow neglecting the air density variation during the battery cell cooling phase. The hydraulic diameter value is 0.018 m for the considered system. The cinematic viscosity related to the initial temperature value is $1{,}5 * 10^{-5}$ m^2/s. By considering the hypothesis described in Section 2.3, the mass flow of the air stream is considered laminar, fixing the *Nusselt number* to 7.54 for the considered duct geometry [53]. From an electrical standpoint, all the cells start at the same *SoC* and *SoH* values set at *10 %* and *100 %* respectively in all simulations. In both the considered *BP* layouts, the battery cells are electrically connected with three rows in parallel, each consisting of five cells in series (*S5P3* configuration).

The considered simulation test aimed to reach demanding high temperature conditions: it involves a Constant Current/Constant Voltage (CC/CV) fast-charging operation followed by a resting period, for an overall test duration of about 3 h. This control mode for charging operations can be easily obtained in a simulation environment using a PI controller that compares maximum charging and actual battery voltage, as reported in [55]. For this test, the constant current charging value is set at a maximum value of 1C, corresponding to 66 A, whereas the considered charging operations are related to a *BP SoC* variation of *0 %* to *100 %*. The complete charging operation is reported in Fig. 18 in

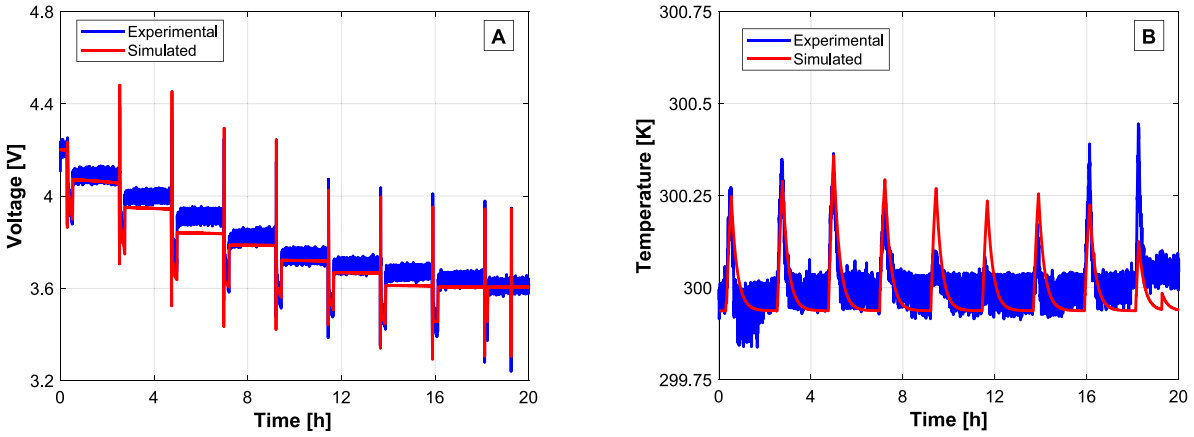

Fig. 15. Voltage (a) and temperature (b) comparison between experimental and simulation data in HPPC.

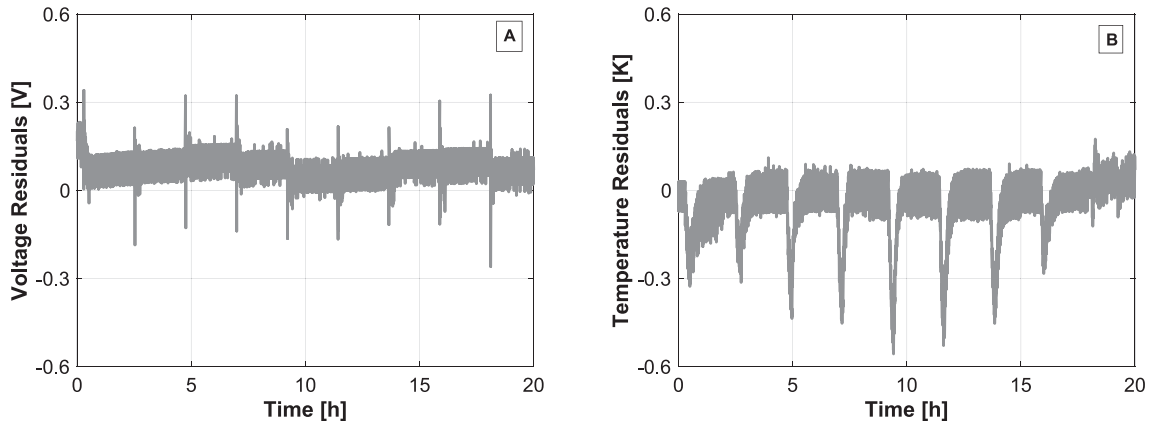

Fig. 16. Voltage and temperature errors in validation tests.

Table 4
Battery pack layout obtained.

Layout	Arrangement
5Rows	*5 rows of three cells*
3Rows	*3 rows of 5 cells*

terms of c-rate and SoC versus time.

In this figure, the charging operation is characterized by a maximum current value of 1C obtained at the beginning of the test. The subsequent decrease in charging current, due to the start of CV mode, obviously involves a reduction in the charging rate and power. After only 45 min, battery charging is mostly complete (~75 %), and the current profile decreases following the typical CC/CV profile until the charging operation stops at around 120 min [56].

For the evaluation of the temperature behavior of the single cell on a 1C charging procedure, simulations are performed with the proposed model by using, as input, the same current profile reported in Fig. 18. The obtained simulation results are compared with the experimental temperature behavior (Fig. 19) evaluated with the experimental set-up described in Section 2.1.

As shown in the figure above, 1C charging operations in the proposed simulation models show good fitting performance in terms of estimated temperature.

At the end of the simulations, the two proposed battery layouts were compared by monitoring the highest temperature hotspots and *BP* temperature distribution. As clearly shown in Fig. 20, these hotspots are located in *BP* cells characterized by lower heat exchange with the external environment.

In both configurations, *NMC* cell number *8* is the *BP* hotspot. In particular, the hottest cell in the first layout is the 2nd cell in the 3rd row, whereas it is the 3rd cell in the 2nd row in the second layout.

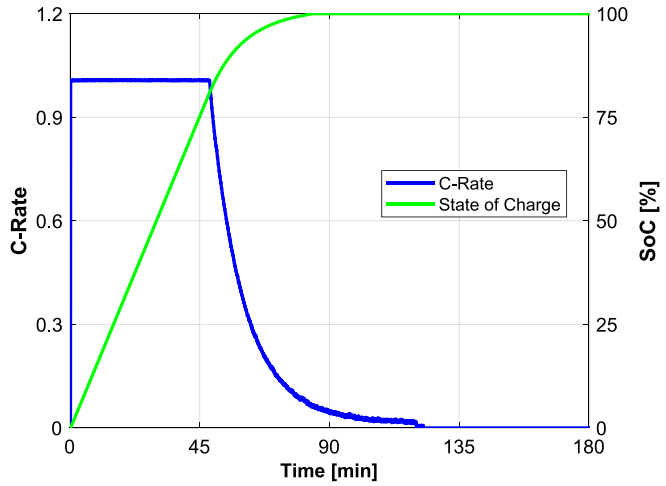

Fig. 18. EV SoC and current demand during 1C charging.

4.2. Comparison between 5Rows and 3Rows layouts without BTMS

The first simulation results are related to the *5Rows* layout. Considering the *BP* modelling assumption, the layout temperature has a symmetrical distribution along the transversal and longitudinal axes. For this reason, the 2nd, 5th and 8th cell temperatures were measured and reported in Fig. 21.

When the electric load is applied during charging operations, the temperature quickly increases moving from the outer to the inner battery cell. The 2nd cell presents the lowest temperature slope thanks to its direct contact with the air-mass at ambient temperature, reaching a maximum value of almost 310 K at the end of the charge. Heat exchange in the 5th and 8th battery cells is less efficient due to overheating of the

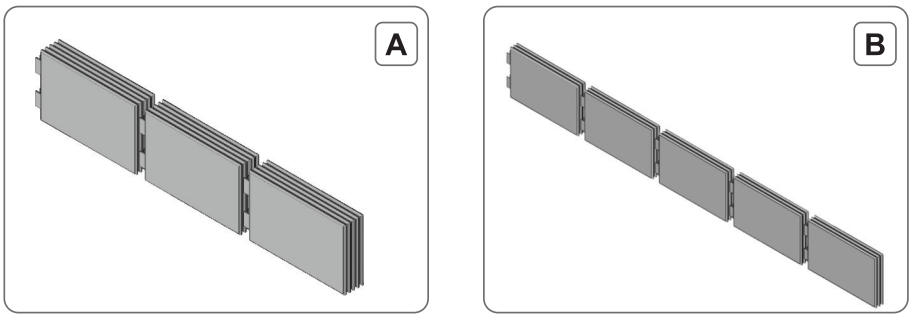

Fig. 17. 5Rows (A) and 3Rows (B) battery pack layouts.

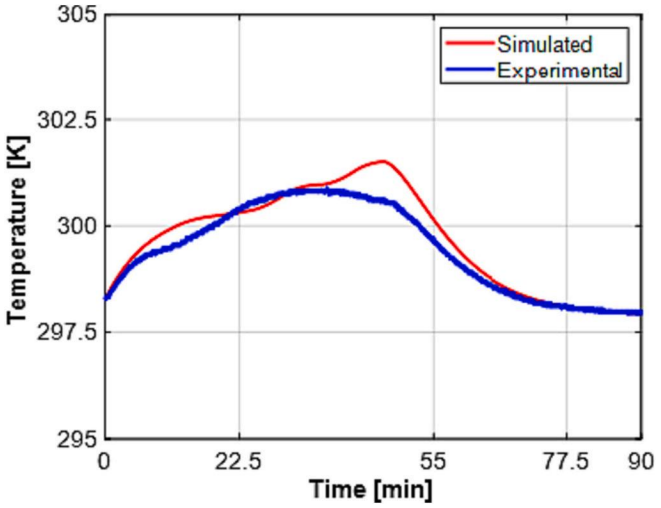

Fig. 19. Experimental and Simulated temperature profile during 1C charging.

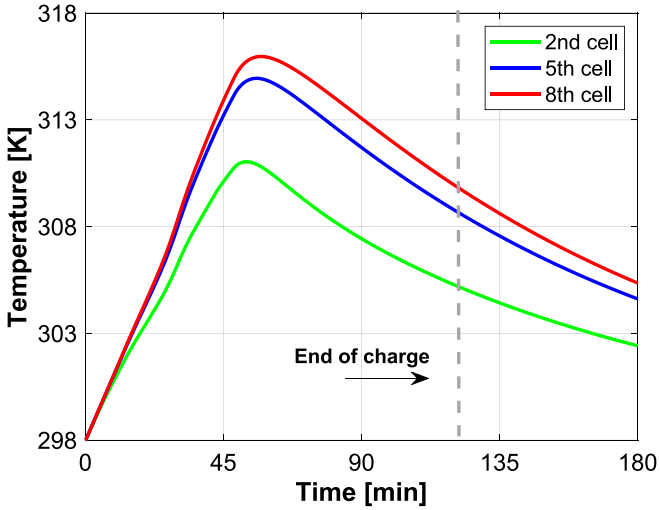

Fig. 21. 2nd, 5th and 8th cell temperature distribution in the 5Rows layout.

air masses around them. Poor dissipation of heat leads to higher maximum temperatures in the inner cells, with both values reaching about 316 K at the end of charge. These effects are also visible in the resting phase, during which the 2nd cell shows a higher temperature decrease gradient. The overall temperature distribution in the layout at the end of charge is shown in Fig. 22.

As expected, the temperature distribution is symmetrical in the longitudinal and transversal layout axes. In conclusion, the *5Rows* layout presents a maximum temperature difference of 6 K between the outer battery cells and the hotspot.

The second simulation results refer to the *3Rows* layout operating with the same electric load. The temperature trends of the 3rd and 8th cells are shown in Fig. 23.

In this configuration, the difference between the hotspot and the other battery cells is smaller than in the previous layout, with a maximum difference of about 2 K. The hottest battery cell in the layout reaches a temperature of 314 K. After the resting phase the temperature of both cells drops below 303 K. This layout solution results in a good thermal distribution within the *BP*, as shown in Fig. 24.

In this case, the *BP's* hotspot is extended to battery cells in the 7th, 8th and 9th positions due to the more uniform temperature distribution inside the energy storage system.

Comparing the thermal distributions of the two *BP* layouts, the *3Rows* layout appears to be a better solution than the *5Rows* layout. Although the lowest battery cell temperatures are quite similar, temperature differences among battery cells are higher in the *5Rows* layout; this may be due to unbalanced battery cell aging phenomena or unbalanced charging/discharging currents inside the BP. In addition, the *3Rows* layout minimizes the maximum temperature of the hotspot, as highlighted in Fig. 25.

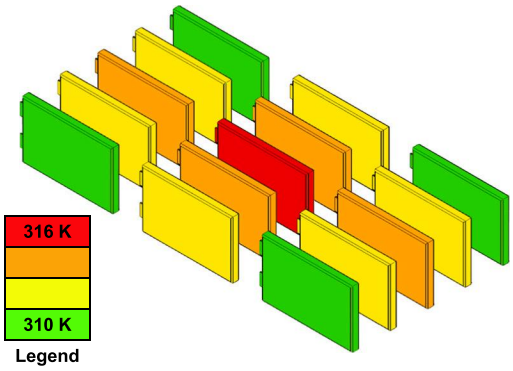

Fig. 22. BP temperature distribution in 5Rows layout after charging operations.

4.3. 3Rows layout with forced air BTMS

Starting from the above consideration, a forced air-cooling system was introduced to evaluate the effects of BTMS on the thermal behavior of the battery cells. Evaluations refer mainly to the *3Rows* layout, since it showed the best thermal performance in terms of maximum cell temperature and temperature distribution. Concerning the geometrical distribution of the cells in the *3Rows* configuration, the air mass provided by the fan was divided into two equal parts directed towards the two rectangular ducts composed of the 1-2 and 2-3 rows. Fig. 26 shows the resulting temperature trends for the 3rd and 8th cells.

In particular, the fan turned on after only 15 min and remained active for about 60 min. During this period, the cooling system managed to keep the maximum hotspot temperature below 307 K. When the

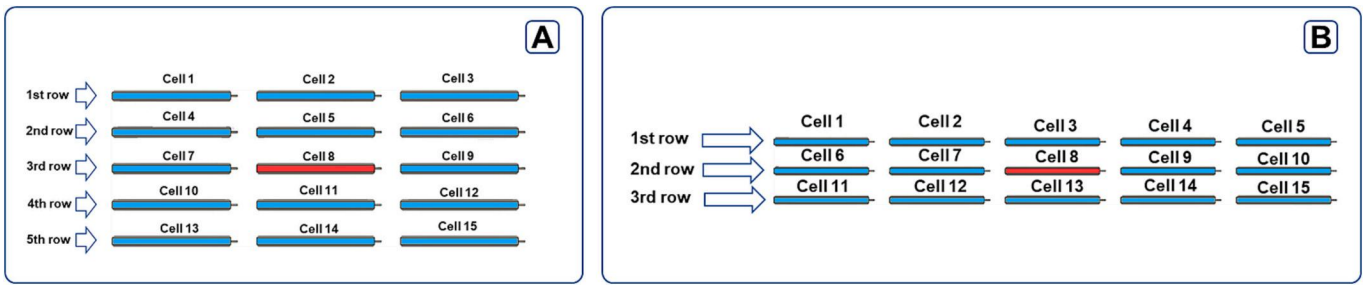

Fig. 20. Hotspots in 5Rows (a) and 3Rows (b) layouts.

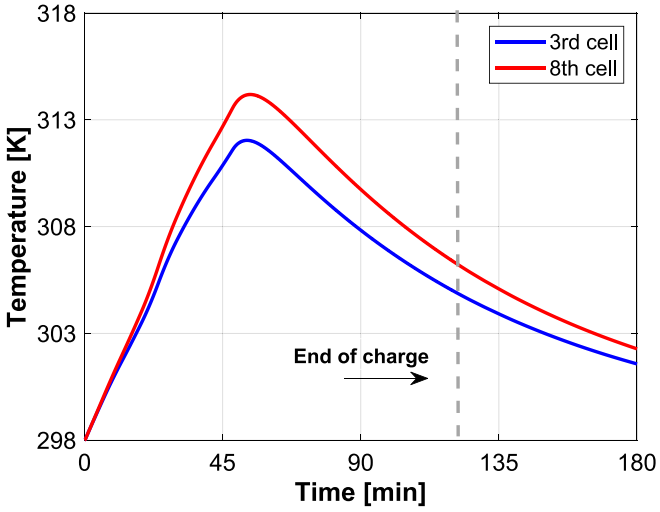

Fig. 23. Longitudinal temperature distribution in the 3Rows layout.

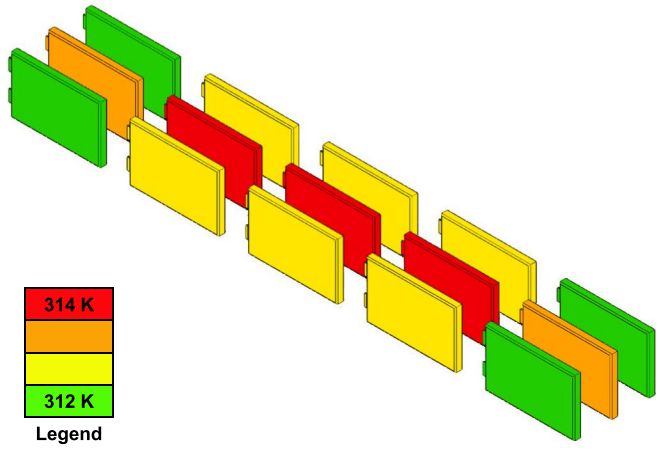

Fig. 24. BP temperature distribution in the 3Rows layout after charging operations.

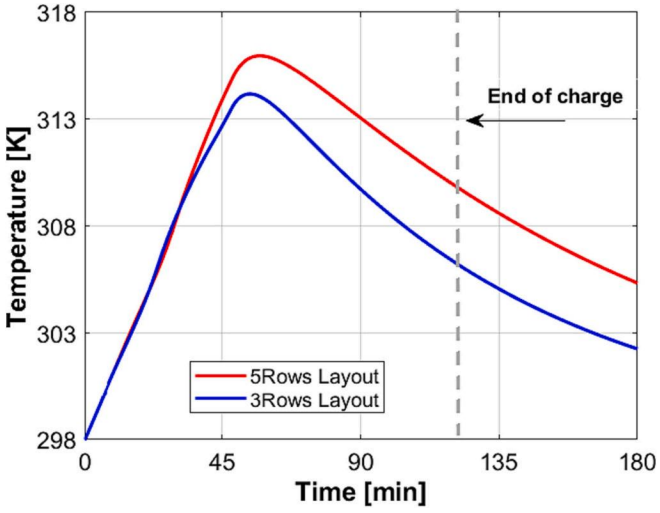

Fig. 25. Comparison between layout hotspots.

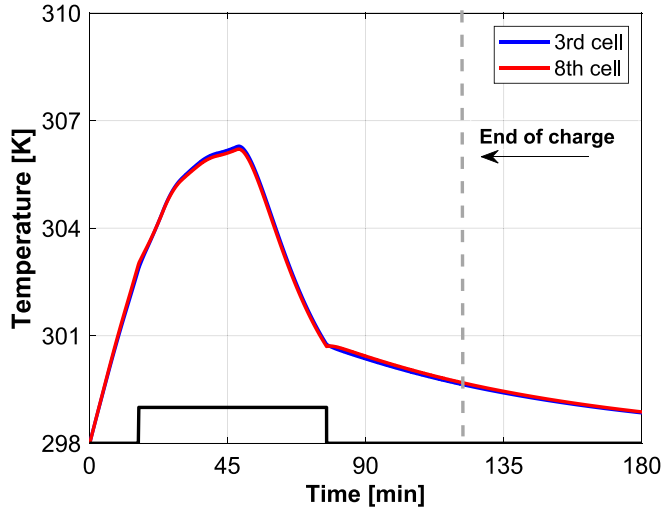

Fig. 26. Longitudinal thermal distribution in the 3Rows layout with air cooling.

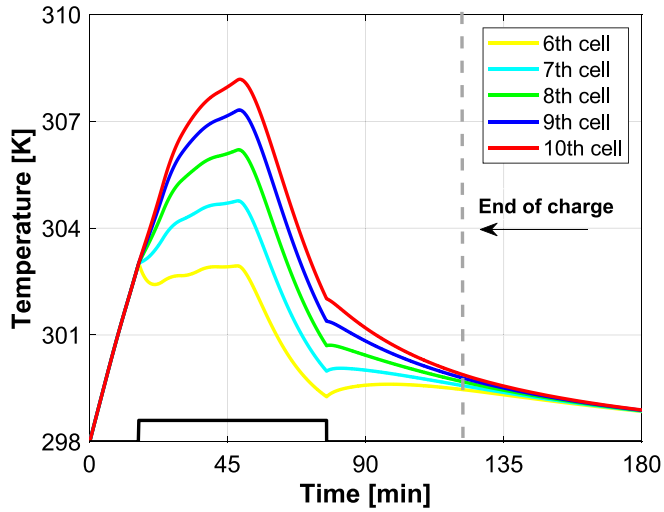

Fig. 27. Transversal temperature distribution in the 3Rows layout with air cooling BTMS.

electrical charging load decreased, the battery cells cooled quickly. The temperature dropped to below the reference temperature of the *BTMS* a few minutes before the load was removed. Note that with the activation of the cooling system, the layout hotspot changed position inside the *BP*, as shown in Fig. 27.

The air mass flow increases in temperature as it passes through the battery cells. For this reason, the 10th battery cell reached a temperature of almost 308 K, the highest in the *BP*. The first battery cells that exchange heat with the fresh cooling medium achieve temperatures of just over 299 K. This condition creates a temperature gradient along the *BP* transversal axis, with a maximum temperature difference of about 5 degrees between the first and the last battery cell in the string. Fig. 28 shows the temperature distribution of the *3Rows* layout configuration, as well as the direction of the air-mass flow.

In conclusion, the implementation of the cooling system in the *3Rows* layout effectively reduced the maximum battery cell temperature inside the *BP*, even though it produced a different asymmetrical temperature distribution. Note that for the considered test, the temperature increase during battery charging operations was contained and acceptable even without a cooling system. However, these conditions refer to brand new cells at 100 % State of Health. The situation changes rapidly when older

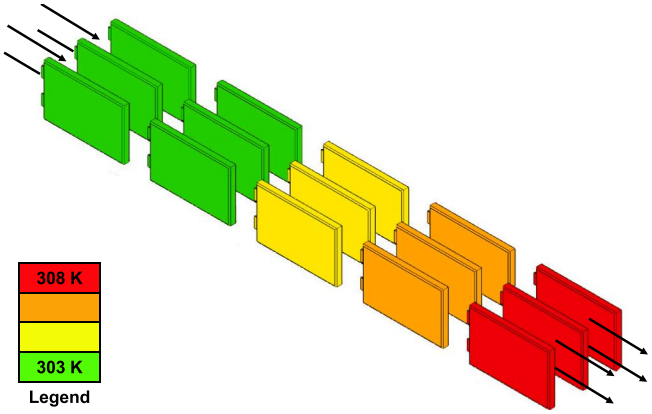

Fig. 28. Temperature distribution of the 3Rows layout with an air cooling BTMS.

cells are considered.

Starting from the above considerations, a last case study focused on the effects of older battery cells on the considered layout. With reference to the *3Rows* layout configuration reported in Fig. 17, the 9th battery cell was considered in an advanced aging state with a *State of Health* equal to 75 %. In this case, the higher inner resistance values of the above cells, calculated using Eq. (1), determined a greater heat generation rate during charging operations compared to the other cells. The presence of an aged cell also influenced the layout temperature distribution due to the development of a new hotspot and a current imbalance between the different *BP* rows. Starting from this configuration, the 2C charging test was repeated under non-cooled operating conditions. Fig. 29 shows the transversal temperature distribution of the 2nd row, where the hottest temperature was recorded.

As shown in the figure above, the hotspot corresponds to the aged battery cell temperature which reaches the highest temperature of about 324 K, whereas new battery cells reach a temperature of around 314 K. In this case, new cells remain at lower temperatures with respect to the values reached when all the battery cells are at the same SoH. This is mainly due to the lower thermal load to be dissipated because of lower current values.

As expected, the BP temperature distribution improves significantly by activating the air-cooling system. The transversal temperature distribution is shown in Fig. 30.

The maximum temperature hotspot value drops below 310 K thanks

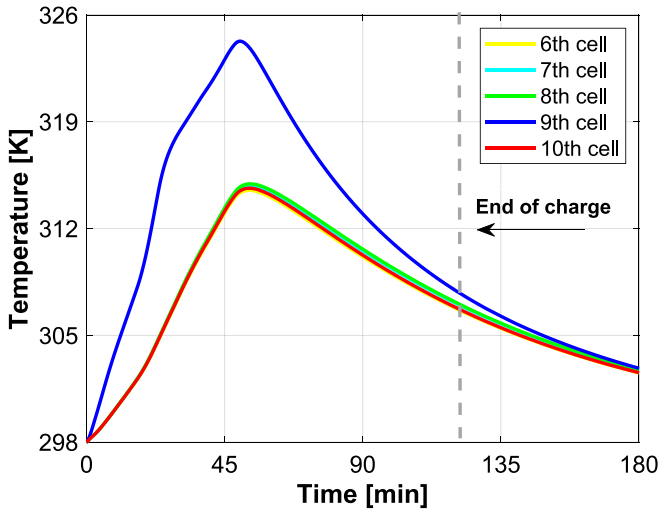

Fig. 29. Transversal thermal distribution in the 3Rows layout with an aged battery cell when the BTMS is deactivated.

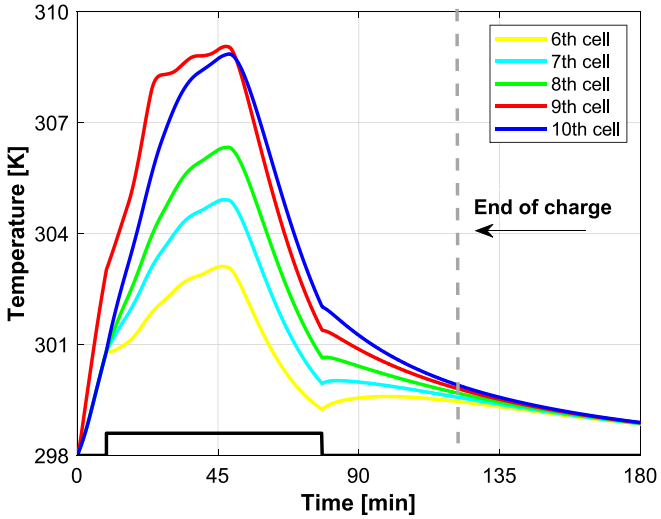

Fig. 30. The transversal temperature distribution in the 3Rows layout with an aged battery cell when the BTMS is activated.

to the higher heat rate caused by the intervention of the BTMS. In this case, the aged battery cell also influences the temperature behavior of the nearest cells, as clearly highlighted by the higher temperatures of the 10th cell with respect to the previous case. In addition, the latter temperature value is limited by the lower current value through the second string due to the difference in internal resistance values. In order to highlight the effectiveness of the cooling system on the aged lithium cell, Fig. 31 shows the temperature trends of the 9th battery cell under all the tested operating conditions.

The figure above highlights temperature trends in the 9th cell during simulations for different SoHs and different cooling conditions. In particular, during the 1C charging test, the maximum temperature of the battery cell increased by 5.37 % under standard conditions when the SoH was 100 % and the cooling system was turned off. Aging affects the rise in temperature during operation. The aged battery cell without a cooling system reached a temperature of 324 K with an 8.72 % rise in temperature. This rapid increase in temperature is of concern because it poses a fire hazard and may lead to a reduction in the remaining useful life of the BP. The situation can be improved by adding an air cooling BTMS that reduces the temperature rise to 5.37 %: this reduces the cell explosion hazard drastically.

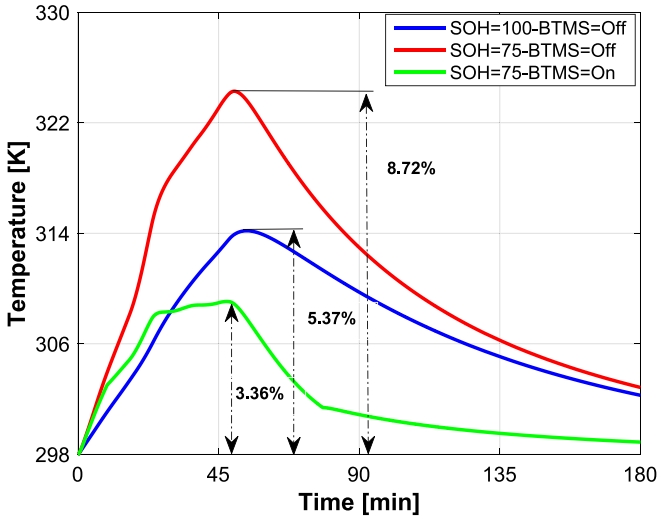

Fig. 31. Comparison between temperature trend of 9th battery cell for all the considered operations.

The reliability of the above results can be considered very high since they were obtained through experimentally validated simulation models. The required computational time, comprehensive of a tic-toc timing analysis on the Simulink numerical model, results in about 2 min. This time is lower in comparison with the requirements of traditional FEM/CFD analysis of about 3 orders of magnitude [44].

The use of models requiring low computational effort and their direct connection with geometric layouts can be very useful to vehicle manufacturers in evaluating the design and sizing of BPs.

5. Conclusions

This study developed a model-based methodology for use in the design of battery packs for automotive applications. This methodology is based on a multi-domain simulation approach to allow electric, thermal and geometric evaluations of different battery pack configurations, with particular reference to Li-NMC technology. The results of this study can be summarized as follows:

- Electro-thermal single-cell models were parametrized and validated on two Li-NMC cells at different States of Health through experimental laboratory activities, also considering heat interactions between cells. The models show good fitting performance with experimental data during both standard and real operating cycles, providing useful information on the expected electric, thermal and aging behavior of the analyzed battery cells.
- A model of an air-cooling system was implemented on the basis of reasonable simplifying assumptions related to air flow and the cross-sectional areas of ducts.
- Based on the above theoretical and experimental evaluations, a complete battery pack numerical model was developed and integrated with a 3D CAD model developed in SolidWorks, allowing easy evaluation of cell layout within the battery pack.
- Simulation results on different battery pack configurations highlighted the effectiveness of the proposed methodology in evaluating the effects of cooling system, aging and cell positioning/arrangement within the battery pack in terms of maximum cell temperature and temperature distribution.

The proposed methodology can be used to analyze different battery pack configurations in a very simple way. Various layouts can be obtained quickly by changing a few parameters and analytical electro-thermal comparison is fast because the battery pack model is created on the basis of lumped parameter multidomain models. The required computational is very low compared to traditional FEM analysis and the accuracy of results is satisfactory for preliminary layout thermal analysis. Battery pack manufacturers can use the proposed methodology to reduce design costs, effort, and time.

Declaration of competing interest

The authors declare that they have no known competing financial interests or personal relationships that could have appeared to influence the work reported in this paper.

Data availability

Data will be made available on request.

Acknowledgements

This research has been partially supported by the European Union-NextGenerationEU - National Sustainable Mobility Center CN00000023, Italian Ministry of University and Research Decree n. 1033—17/06/2022, Spoke 12, CUP B43C22000440001.

References

[1] B. Scrosati, J. Garche, Lithium batteries: status, prospects and future, J. Power Sources 195 (9) (2010) 2419–2430.
[2] Y. Tang, W. Yuan, M. Pan, Z. Wan, Experimental investigation on the dynamic performance of a hybrid PEM fuel cell/battery system for lightweight electric vehicle application, Appl. Energy 88 (1) (2011) 68–76.
[3] W. Van Schalkwijk, B. Scrosati, Advances in Lithium-Ion Batteries Introduction, Springer US, 2002, pp. 1–5.
[4] S. Amjad, S. Neelakrishnan, R. Rudramoorthy, Review of design considerations and technological challenges for successful development and deployment of plug-in hybrid electric vehicles, Renew. Sust. Energ. Rev. 14 (3) (2010) 1104–1110.
[5] R. Wagner, N. Preschitschek, S. Passerini, J. Leker, M. Winter, Current research trends and prospects among the various materials and designs used in lithium-based batteries, J. Appl. Electrochem. 43 (2013) 481–496.
[6] S. Manzetti, F. Mariasiu, Electric vehicle battery technologies: from present state to future systems, Renew. Sust. Energ. Rev. 51 (2015) 1004–1012.
[7] A. Mahmoudzadeh Andwaria, A. Pesiridisa, S. Rajooc, R. Martinez-Botasd, V. Esfahanianb, A review of battery electric vehicle technology and readiness levels, Renew. Sust. Energ. Rev. 78 (2017) 414–430.
[8] W. Waag, S. Käbitz, D.U. Sauer, Experimental investigation of the lithium-ion battery impedance characteristic at various conditions and aging states and its influence on the application, Appl. Energy 102 (2013) 885–897.
[9] X. Yu, Z. Lu, L. Zhang, L. Wei, X. Cui, L. Jin, Experimental study on transient thermal characteristics of stagger-a ranged lithium-ion battery pack with air cooling strategy, Int. J. Heat Mass Transf. 143 (2019), 118576.
[10] L. Lu, X. Han, J. Li, J. Hua, M. Ouyang, A review on the key issues for lithium-ion battery management in electric vehicles, J. Power Sources 226 (2013) 272–288.
[11] F.M. Nizam Uddin Khan, Mohammad G. Rasul, A.S.M. Sayem, Nirmal K. Mandal, Design and optimization of lithium-ion battery as an efficient energy storage device for electric vehicles: a comprehensive review, J. Energy Storage 71 (2023), 108033.
[12] R. Kumar, V. Goel, A study on thermal management system of lithium-ion batteries for electrical vehicles: a critical review, J. Energy Storage 71 (2023), 108025.
[13] F. Zhang, P. Wang, M. Yi, Design optimization of forced air-cooled lithium-ion battery module based on multi-vents, J. Energy Storage 40 (2021), 102781.
[14] T. Ebbs-Picken, C.M. Da Silva, C.H. Amon, Design optimization methodologies applied to battery thermal management systems: a review, J. Energy Storage 67 (2023), 107460.
[15] S. Tamilselvi, S. Gunasundari, N. Karuppiah, R.K.A. Razak, S. Madhusudan, V. M. Nagarajan, A. Afzal, A review on battery modelling techniques, Sustainability 13 (18) (2021), 10042.
[16] A. Fotouhi, D.J. Auger, K. Propp, S. Longo, M. Wild, A review on electric vehicle battery modelling: from Lithium-ion toward Lithium–Sulphur, Renew. Sust. Energ. Rev. 56 (2016) 1008–1021.
[17] S.J. Moura, N.A. Chaturvedi, M. Krstić, Adaptive partial differential equation observer for battery state-of-charge/state-of-health estimation via an electrochemical model, J. Dyn. Syst. Meas. Control. 136 (1) (2014).
[18] M.C. Glass, Battery electrochemical nonlinear/dynamic SPICE model, in: IECEC 96, Proceedings of the 31st Intersociety Energy Conversion Engineering Conference vol. 1, IEEE, 1996, pp. 292–297.
[19] A. Sarmadian, W.D. Widanage, B. Shollock, F. Restuccia, Experimentally verified thermal-electrochemical simulations of a cylindrical battery using physics-based, simplified and generalised lumped models, J. Energy Storage 70 (2023), 107910.
[20] S. Taslimi Taleghani, B. Marcos, G. Lantagne, Modeling and simulation of a commercial graphite-$LiFePO_4$ cell in a full range of C-rates, J. Appl. Electrochem. 48 (2018) 1389–1400.
[21] A. Schmidt, D. Oehler, A. Weber, T. Wetzel, E. Ivers-Tiffée, A multi scale multi domain model for large format lithium-ion batteries, Electrochim. Acta 393 (2021), 139046.
[22] A.G. Kashkooli, H. Fathiannasab, Z. Mao, Z. Chen, Application of artificial intelligence to state-of-charge and state-of-health estimation of calendar-aged lithium-ion pouch cells, J. Electrochem. Soc. 166 (4) (2019) A605.
[23] H. Chaoui, C.C. Ibe-Ekeocha, H. Gualous, Aging prediction and state of charge estimation of a $LiFePO_4$ battery using input time-delayed neural networks, Electr. Power Syst. Res. 146 (2017) 189–197.
[24] Z. Wang, S. Zeng, J. Guo, T. Qin, Remaining capacity estimation of lithium-ion batteries based on the constant voltage charging profile, PLoS One 13 (7) (2018), e0200169.
[25] H. Sheng, J. Xiao, Electric vehicle state of charge estimation: nonlinear correlation and fuzzy support vector machine, J. Power Sources 281 (2015) 131–137.
[26] F. Eltoumi, A. Badji, M. Becherif, H.S. Ramadan, Experimental identification using equivalent circuit model for lithium-ion battery, Int. J. Emerg. Electr. Power Syst. 19 (3) (2018), 2017-0210.
[27] Y. Yu, N. Narayan, V. Vega-Garita, J. Popovic-Gerber, Z. Qin, M. Wagemaker, M. Zeman, Constructing accurate equivalent electrical circuit models of lithium iron phosphate and lead–acid battery cells for solar home system applications, Energies 11 (9) (2018) 2305.
[28] L. Zhang, H. Peng, Z. Ning, Z. Mu, C. Sun, Comparative research on RC equivalent circuit models for lithium-ion batteries of electric vehicles, Appl. Sci. 7 (2017) 1002.
[29] D. Bernardi, E. Pawlikowski, J. Newman, A general energy balance for battery systems, Electrochem. Soc. 132 (1) (1985).
[30] V.G. Choudhari, A.S. Dhoble, T.M. Sathe, A review on effect of heat generation and various thermal management systems for lithium ion battery used for electric vehicle, J. Energy Storage 32 (2020), 101729.

[31] Simone Barcellona, Luigi Piegari, Lithium-ion battery models and parameter identification techniques, Energies 10 (12) (2017), 2007.
[32] Y. Inui*, Y. Kobayashi, Y. Watanabe, Y. Watase, Y. Kitamura, Simulation of temperature distribution in cylindrical and prismatic lithium ion secondary batteries, Energy Convers. Manag. 48 (2007) 2103–2109.
[33] H. Shi, L. Wang, S. Wang, C. Fernandez, X. Xiong, B.E. Dablu, W. Xu, A novel lumped thermal characteristic modeling strategy for the online adaptive temperature and parameter co-estimation of vehicle lithium-ion batteries, J. Energy Storage 50 (2022), 104309.
[34] A. Broatch, P. Olmeda, X. Margot, L. Agizza, A generalized methodology for lithium-ion cells characterization and lumped electro-thermal modelling, Appl. Therm. Eng. 217 (2022), 119174.
[35] X. Lin, X.E. Perez, S. Mohan, J.B. Siegel, A.G. Stefanopoulou, Yi Ding, M. P. Castanier, A lumped-parameter electro-thermal model for cylindrical batteries, J. Power Sources 2014 (257) (2014) 1–11.
[36] C. Forgez, D.V. Do, G. Friedrich, M. Morcrette, C. Delacourt, Thermal modeling of a cylindrical $LiFePO_4$/graphite lithium-ion battery, J. Power Sources 195 (9) (2010) 2961–2968.
[37] C. Zheng, M. Bricogne, J. Le Duigou, B. Eynard, Survey on mechatronic engineering: a focus on design methods and product models, Adv. Eng. Inform. (2014) 241–257.
[38] L. Jun, W. Guochen, L. Yanyan, Multi-domain modeling based on modelica, in: MATEC Web of Conference, 2016.
[39] A. Bordes, D.L. Danilov, P. Desprez, A. Lecocq, G. Marlair, B. Truchot, S. Lamontarana, A holistic contribution to fast innovation in electric vehicles: an overview of the DEMOBASE research project, ETransportation 11 (2022), 100144.
[40] B.R. Kim, T.N. Nguyen, C.W. Park, Cooling performance of thermal management system for lithium-ion batteries using two types of cold plate: experiment and MATLAB/Simulink-Simscape simulation, Int. Commun. Heat Mass Transf. 145 (2023), 106816.
[41] K. Smith, G.H. Kim, E. Darcy, A. Pesaran, Thermal/electrical modeling for abuse-tolerant design of lithium ion modules, Int. J. Energy Res. 34 (2) (2010) 204–215.
[42] Z. Shung-bo, H.E. Xuan, L. Nan-chong, S. Yang-jie, G. Qiang, Improving the air-cooling performance for lithium-ion battery packs by changing the air flow pattern, Appl. Therm. Eng. 221 (2022), 119825.
[43] C.C. Okaeme, C. Yang, A. Saxon, J.A. Lustbader, D. Villeneuve, C. Mac, T. Reed, Thermal design analysis for SuperTruck II lithium-titanate battery pack, J. Energy Storage 56 (2022), 105753.
[44] P. Cicconi, P. Kumar, Design approaches for Li-ion battery packs: a review, J. Energy Storage 73 (2023), 109197.
[45] P. Jindal, P. Sharma, M. Kundu, S. Singh, D. Shukla, K. Pawar, V.J. Breedon P., Computational Fluid Dynamics (CFD) analysis of Graphene Nanoplatelets for the cooling of a multiple tier Li-ion battery pack, Therm. Sci. Eng. Prog. 31 (2022), 101282.
[46] M.S. Hosen, P. Yadav, J. Van Mierlo, M. Berecibar, A post-mortem study case of a dynamically aged commercial NMC cell, Energies 16 (3) (2023) 1046.
[47] A.J. Warnecke, D.U. Sauer, M. Danzer, Degradation Mechanisms in NMC-based Lithium-Ion Batteries (No. RWTH-2017-09646), Institut für Stromrichtertechnik und Elektrische Antriebe, 2017.
[48] C. Capasso, O. Veneri, Experimental analysis on the performance of lithium-based batteries for road full electric and hybrid vehicles, Appl. Energy 136 (2014) 921–930.
[49] Y.A. Cengel, Introduction to Thermodynamics and Heat Transfer vol. 846, McGraw-Hill, New York, 1997.
[50] G. Fathoni, S.A. Widayat, P.A. Topan, A. Jalil, A.I. Cahyadi, O. Wahyunggoro, Comparison of State-of-Charge (SOC) estimation performance based on three popular methods: Coulomb counting, open circuit voltage, and Kalman filter, in: 2017 2nd International Conference on Automation, Cognitive Science, Optics, Micro Electro-Mechanical System, and Information Technology (ICACOMIT), 2017, pp. 70–74.
[51] L. Fang, J. Li, B. Peng, Online estimation and error analysis of both SOC and SOH of Lithium-ion battery based on DEKF method, Energy Procedia 158 (2019) 3008–3013.
[52] Y. Xiao, J. Wen, L. Yao, J. Zheng, Z. Fang, Y. Shen, A comprehensive review of the lithium-ion battery state of health prognosis methods combining aging mechanism analysis, J. Energy Storage 65 (2023), 107347.
[53] Y. Cengel, Heat Transfer, in: A Practical Approach, McGraw Hill, 2022, 978-0072458930.
[54] Y. Cai, Y. Che, H. Li, M. Jiang, P. Qin, Electro-thermal model for lithium-ion battery simulations, J. Power Electron. 21 (10) (2021) 1530–1541.
[55] O. Veneri, C. Capasso, D. Iannuzzi, Experimental evaluation of DC charging architecture for fully-electrified low-power two-wheeler, Appl. Energy 162 (2016) 1428–1438.
[56] W. Shen, T.T. Vo, A. Kapoor, Charging algorithms of lithium-ion batteries: an overview, in: 7th IEEE Conference on Industrial Electronics and Applications (ICIEA), IEEE, 2012, pp. 1567–1572.